

Detectability Evaluation of Attributes Anomaly for Electronic Components Using Pulsed Thermography

Haochen Liu ^a, Lawrence Tinsley ^a, Pavan Addepalli ^a, Xiaochen Liu ^a, Andrew Starr ^a and Yifan Zhao ^{a*}

^a School of Aerospace, Transport and Manufacturing, Cranfield University, Cranfield, MK43 0AL, UK

* Corresponding author. Tel.: +44(0) 1234754729; *E-mail address*: yifan.zhao@cranfield.ac.uk

Abstract

Counterfeit Electronic Components (CECs) pose a serious threat to all intellectual properties and bring fatal failure to the key industrial systems. This paper initiates the exploration of the prospect of CEC detection using pulsed thermography (PT) by proposing a detectability evaluation method for material and structural anomalies in CECs. Firstly, a numerical Finite Element Modelling (FEM) simulation approach of CEC detection using PT was established to predict the thermal response of electronic components under the heat excitation. Then, by experimental validation, FEM simulates multiple models with attribute deviations in mould compound conductivity, mould compound volumetric heat capacity and die size respectively considering experimental noise. Secondly, based on principal components analysis (PCA), the gradients of the 1st and 2nd principal components are extracted and identified as two promising classification features of distinguishing the deviation models. Thirdly, a supervised machine learning-based method was applied to classify the features to identify the range of detectability. By defining the 90% of classification accuracy as the detectable threshold, the detectability ranges of deviation in three attributes have been quantitatively evaluated respectively. The promising results suggest that PT can act as a concise, operable and cost-efficient tool for CECs screening which has the potential to be embedded in the initial large scale screening stage for anti-counterfeit.

Keywords

Counterfeit electronic components; Attributes anomaly; Pulsed thermography; Detectability evaluation; Machine learning;

1. Introduction

Counterfeit Electronic Components (CECs) have become a challenge and major threat to the semiconductor supply chain for civil, industrial and defence purposes globally. CECs and corresponding illegal trade rose from \$461 billion to \$509 billion between 2017 and 2019 [1], amounting to as much as 3.3% of the world trade of intellectual property. Counterfeits not only defraud customers, but also present a significant drain on legitimate manufacturing in the electronics industry, diverting funds from brand owners who research and develop new products, and lending potency to organised crime [2]. Due to their lower quality, efficiency, increase in malfunctions and unreliability, CECs are well known to cause catastrophic injury and failure to operators and critical systems, creating billions of dollars losses in manufacturing, transport, aviation, power generation, and cybersecurity every year [3].

The CECs can be defined as Electronic Components (ECs) with 1) unauthorised copy; 2) inconformity to the original component manufacturer (OCM) design, models or standards; 3) unauthorised source; 4) broken, defective, or used OCM products; 5) fraudulent markings or documentation [4, 5]. Figure 1 shows common counterfeit forms embedded in the supply chain and the corresponding defects causing them. Multiple defect types are related to the physical properties of ECs such as the material, internal structural anomaly (e.g. missing or broken die/wires, improper material, dimension and corroded or oxidated mould packaging, etc.) and electronic malfunctions (e.g. current leak, transistor variation, improper electrical heat emission etc.), while others are related to external markings and trade paperwork (e.g. sanding marking, forged shipping label or paperwork, etc.). In response, a few typical inspection techniques aimed at testing the interior and exterior integrity, and electronic functionality, have emerged to screen ECs in the supply chain, which can be broadly categorised as either physical or electrical tests [6, 7]. However, subjecting to the advantages

and limitations in inspection speed, cost and capability, stakeholders normally have to deploy manifold inspection methods in multiple supply chain stages to perfect exhaustive screening [8, 9]. For instance, as an exterior physical inspection, random visual spot-checking is popular for initial screening due to simplicity but it may result in a high uncertainty regarding the pass/failure product ratio if the sampling in a large number of chips is not appropriate [10]. X-Ray imaging [11] and Terahertz spectroscopy testings [12] are capable to analyse the accurate internal physical properties such as wires, circuit joint and package material, but are limited by low throughput, a high capital cost per inspection unit, or overly sophisticated methodology for unskilled operators. Electrical testing like burn-in testing, current leakage testing and function verification are able to detect electrical malfunctions but incapable to detect structural defects and aged components [13]. Therefore, an intuitive, non-contact, high cost-efficiency non-destructive inspection technique is highly demanded in the first stage

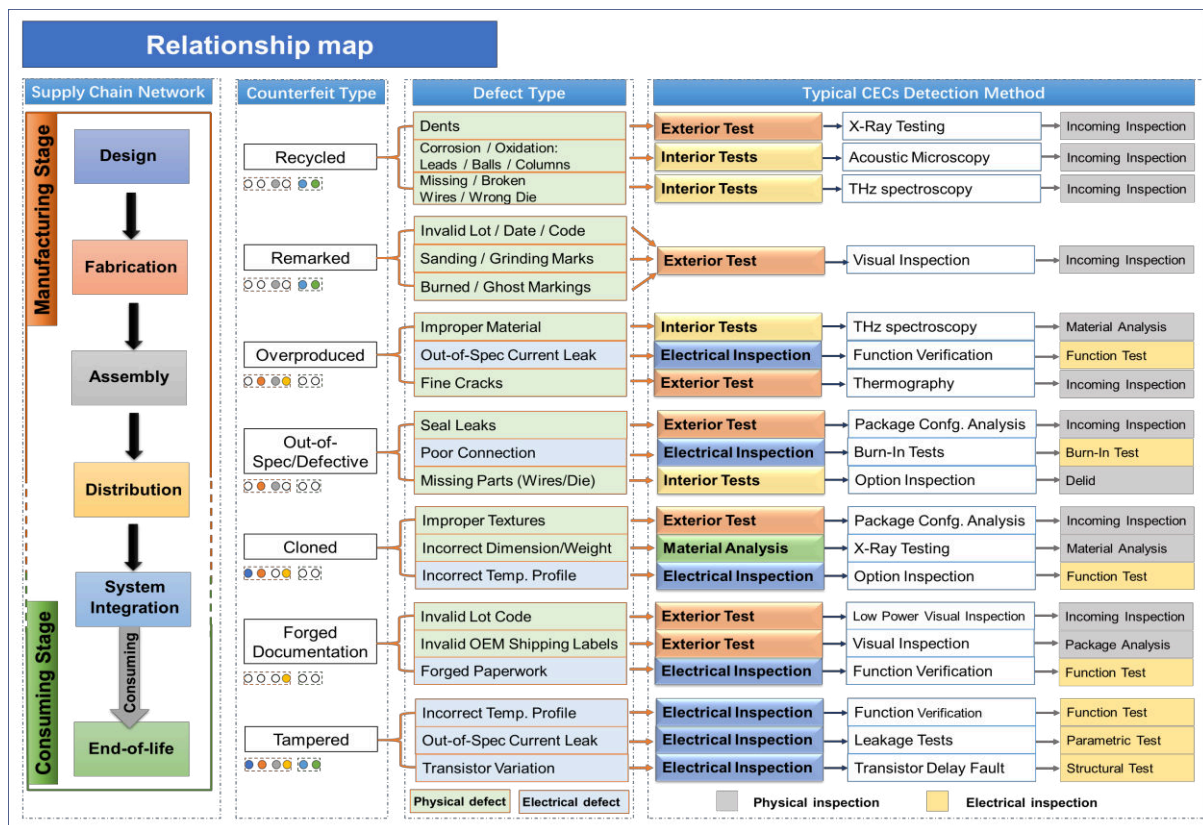


Figure 1. Counterfeit types and typical detection methods in the entire supply chain.

large scale inspection for reducing the proliferation of UVECs.

This research focuses on material and structural defects in CECs. For a conventional type of EC (shown in Figure 2(a)), five fundamental elements including die, mould compound, lead frame, pins and wiring typically feature as their main design elements. Most of physically unqualified CECs commonly have defects or anomalies in these five elements. For example, disqualified manufacturing may use an undersized die for cost-saving but results in a wrong die counterfeit [14]. Broken interior leads or wires may lead to low performance or partial malfunctions counterfeit [15]. Aged or over usage life counterfeits would often incur package material degradation in either the mould compound or die, caused by long-term thermal fatigue cycles [16]. Figure 2(b) presents a comparison between an authentic and a counterfeit EC in X-Ray images. The differences in mould material (indicated by the variation of grayscale intensity), lead frame layout and die size prove multiple counterfeit types mentioned above.

Non-destructive Evaluation (NDE) techniques have been widely used and play an important role in structure maintenance and degradation-assessment. Among the diverse range of inspection methods, infrared thermography (IRT) is a powerful and promising technique due to its advantages of rapid, non-contact inspection approach and its ability to produce intuitive inspection images [17]. IRT can be divided into two modes: active and passive. Active thermography encompasses different approaches according to the choice of heat source, including flash [18], laser [19], eddy current [20] and ultrasonic vibration. The heating mode differs between pulse, lock-in and modulated patterns, selected according to the appropriate type of defect. The eddy current thermography has been proven to be effective for detecting the degradations of insulated gate bipolar transistor circuit module especially for bond wires and layers joint [21]. Compared to eddy current and laser thermography, the

Pulsed Thermography (PT) employing instantaneous flash is highly competent with remote excitation distance and larger heating area for inspection, such a characteristic is attractive for ECs inspection because it allows inspecting a significant number of components simultaneously, facilitating a rapid and cost-efficient inspection per part. In addition, the relatively concision, operability and low-budget contribute that the PT system can be deployed and embedded into multiple stages on the supply chain. Therefore, development of such a rapid, reliable and cost-efficient PT inspection for CECs will provide a powerful tool for CECs detection, especially in the initial large scale screening stage.

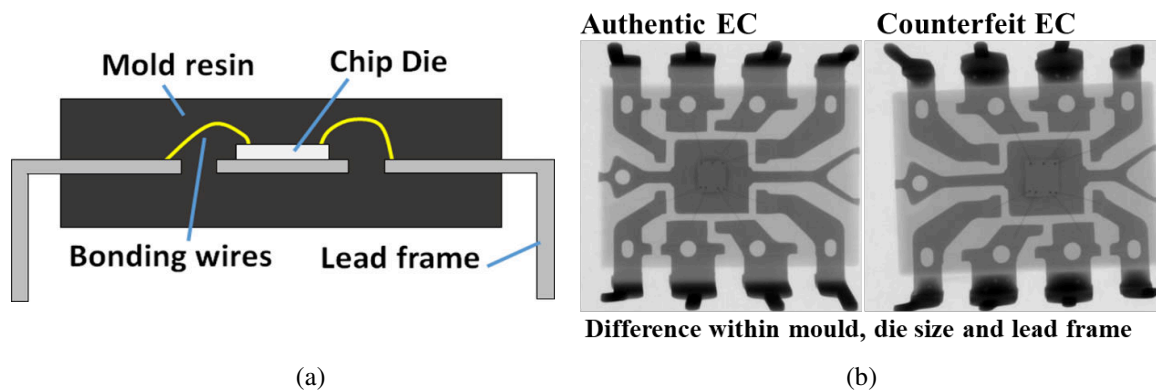


Figure 2. Typical structure of EC. (a) Simplified structure of a conventional dual in-line package (DIP) electronic component; (b) Comparison of authentic and counterfeit ECs in X-ray images.

Quantitative damage characterisation in single metal and composite structures by sizing shape and depth has been well studied and proven to be effective by PT [22-25]. These researches are performed based on the assumption that the targeted defects are detectable. However, as a new inspection technique employed to anti-counterfeits, the thermal response and corresponding detectability using PT for different types of material and structure anomaly are still unknown. It is therefore essential to clarify the detectability of each type of counterfeit anomaly or defect in thermography, in order to ascertain the detectability of the technique for a given counterfeit-derived anomaly. This work aims to evaluate the detectability of PT for anomalies in mould compound thermal properties and die chip size;

enabling the boundaries of detectability to be established before the experiment, providing a means to assess the method's capability for several defect types.

To quantitatively investigate the detectability of a specific anomaly parameter, two challenges are crucial to this investigation. The first is that the counterfeit samples with standardised levels of anomaly are difficult to collect. To address this challenge, the modelling simulation for PT thermal response of CECs is proposed in this research. To model the ECs, several studies have been investigated to predict the thermal temperature response of the die part for electronic performance evaluation and manufacturing design. Initial researches focus on the electro-thermal analysis of the interior chip and die, where the heat source is generated by electrical power charging the chip [26]. Leila *et al.* proposed an analytical modelling solution for steady-state and transient temperature field in a type of vertically stacked die [27]. However, the excitation manner, heating position and temperature behaviour in these studies are different from the proposed PT inspection of CECs, therefore a simulation investigation for PT thermal response of CECs is necessary. The second challenge for evaluating the PT technique involves the effective decision-making criteria for judging the detectability of mould compound material and die structure from PT, which is still unclear. The use of a machine learning classification algorithm to characterise the damage has been attracting increasing attention in maintenance industries [28]; studies that have been conducted to automatically determine the defects in material [29] and deterioration in infrastructure [30] where traditional NDE techniques such as ultrasonic testing, radar, acoustic emission, infrared thermography and Terahertz spectroscopy have been used [31, 32]. In material identification, Aujeszky *et al.* proposed a material classification approach using laser thermography that can differentiate a variety of materials such as plastic, coal, marble etc [33]. However, the investigated objects are single material with homogenous

distribution and are excited by a small laser spot, which is not necessarily suitable for the CECs with complex structures inspected in PT. To discriminate the detectability of a certain counterfeit type, with the uncertainties and errors associated with the inspection itself, it is essential to establish a group of anomaly features and address the classification accuracy to resolve the smallest limitation of anomaly that can be captured by PT.

This paper is an effort to answer the aforementioned challenges and thus proposes a numerical approach to predict the thermal response of the standardised level of counterfeit anomalies, and then introduces a machine learning classification approach to estimate the detectability of the material and interior structural anomalies of CECs. This paper is organised as follows: Section 2 presents the overall methodology and the numerical modelling of ECs in PT. In Section 3, feature extraction and machine learning-based classification are introduced. Section 4 presents the results and discussion, and conclusions are given in Section 5.

2. Methods

2.1 Overall Methodology

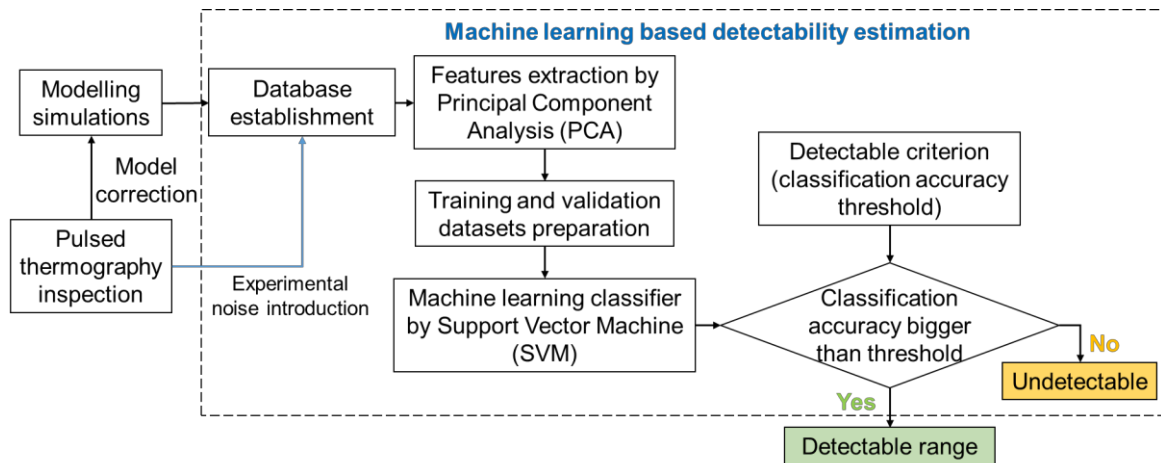


Figure 3. The principle of the proposed methodology

Figure 3 shows an overview of the proposed methodology to investigate the detectability of various counterfeit types for ECs using PT.

Initially, a model-based finite element model (FEM) is established to predict the temperature response of ECs after the heating, and then an experimental test of PT is performed to inform the selection of parameters in FEM and evaluate the experimental noise for refining the model. By simulating a series of standardised levels of anomalous models and introducing different levels of noise, the datasets to represent the thermal behaviour of the inspected CECs are established. Secondly, the simulated datasets are processed with principal component analysis (PCA) to extract the key features. These feature datasets are carefully prepared to form the training and validation datasets for developing and validating a machine learning classifier. Then the classifier aims to differentiate and label the anomalous models from the reference model. Through defining an appropriate threshold, the classification accuracy of each clustered result can in return provide an indicator of detectable range of the anomalous parameters referring to counterfeits against the reference parameters.

2.2 Finite element modelling and simulation

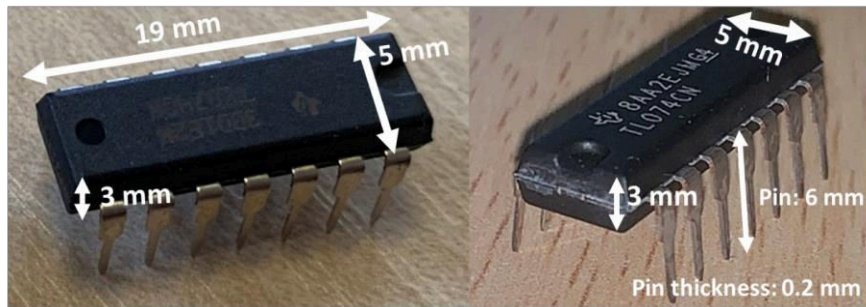


Figure 4. The dimensions of investigated EC.

In this research, a typical EC fabricated with dual in-line package shown in Figure 4 is adopted as a typical use case. A simplified 3D model is established with a four-layer structure, shown in Figure 5, which consists of double mould compound layers, lead frame layer and die layer, representing a conventional EC. The detailed structures of lead frame,

pins and die are modelled as homogenous layers. The thermal properties of material in each layer are approximately estimated using the commonly used material [20] shown in Table 1.

Table 1 Material thermal properties

Component (Material type)	Mould conductivity	Mould volumetric heat capacity
Mould Compound (Mould resin)	7.2 W/(m·K)	1.33×10 ⁶ J/K/m ³
Lead frame and pins (Copper)	3.85×10 ² W/(m·K)	3.45×10 ⁶ J/K/m ³
Die (Silicon)	1.30×10 ² W/(m·K)	1.65×10 ⁶ J/K/m ³

The transient thermal response of PT inspection can be simulated by the heat conduction equation shown in Eq. (1).

$$\kappa \{\nabla\}^T \{\nabla\} T - \rho c \dot{T} = -Q|_{\Gamma} \quad (1)$$

$$[K]\{T\} + [C]\{\dot{T}\} = \{Q\} \quad (2)$$

where T and $\{\nabla\}$ denote the temperature and gradient vector and $-Q|_{\Gamma}$ is the excitation heat flux applied on the surface. κ , ρ and c denote the heat conductivity, density and specific heat of material respectively. Assuming no heat loss, the temperature of the tested sample can be conducted by the FEM governing equation Eq. (2), where $[K]$, $[C]$ and $\{Q\}$ stand for coefficient stiffness matrix of conductivity, volumetric specific heat and excitation heat source respectively. To solve Eq. (2), a time-domain integration solver was employed as (3) [34]. In (3), $\zeta=0.5$ is a convergence parameter that controls the calculation stability and accuracy. Additionally, to calculate the surface temperature response, the model is based on the following assumptions:

- (1) The material selected is homogenous and isotropic.
- (2) The ambient thermal equilibrium conditions are used.
- (3) The constant thermal properties are used and the thermal expansion effect is neglected.
- (4) Non-adiabatic surrounding condition is adopted and the EC model is surrounded by air elements.

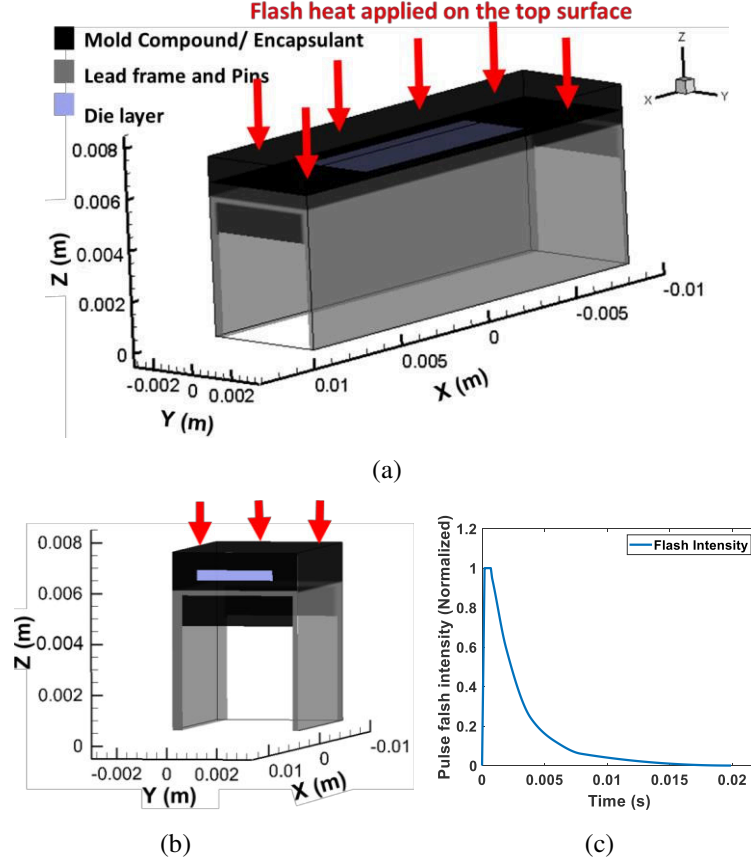


Figure 5. The modelling of PT inspection. (a) The established model of target EC; (b) A slice of the model in X direction; (c) The flash intensity of the heating pulse.

$$\left[[K](1-\zeta) + \frac{[C]}{\Delta t} \right] \{ \dot{T} \}_{t+\Delta t} = \{ Q \}_{t+\Delta t} + \left[\frac{[C]}{\Delta t} - \zeta [K] \right] \{ T \}_t \quad (3)$$

In PT, a homogenous flash is used to heat the top surface of the sample. Considering the smaller size of EC, the heat energy intensity induced on single EC can be regarded as uniform heating. The temporal pulse wave of heating is as shown in Figure 5(c). The pulse peak of heat flux density applied on the surface elements is $5.0 \times 10^4 \text{ W/m}^2$.

2.3 Model validation through experimental tests

To validate the simulation, an experimental test was performed on a group of representative EC samples; in this case common operational amplifiers. These were randomly selected to represent frequently used electronic components that also provide a comparatively

large surface area. This consideration is significant in the early stages of the work for enabling a simple comparison between simulation results and captured data, before applying it to real CECs and their genuine counterparts. The experimental setup of PT is illustrated in Figure 6(a), where a short and high-energy light pulse was projected onto the sample surface through double flash lamps. An infrared camera controlled by a PC captures the time-dependent response of the sample surface temperature. The experiments were conducted using the Thermoscope® II pulsed-active thermography system (see in Figure 6(b)) that comprises of two capacitor bank powered Xenon flash lamps mounted in an internally reflective hood and a desktop PC to capture and store data. A FLIR SC7000 series infrared (IR) radiometer operating between 3-5.1 μm and a spatial resolution of 640×510 pixels was used to perform the inspection with a sampling framerate of 100 Hz. The samples were placed with their surface perpendicular to the IR camera's line of sight at 250 mm from the lens. The sample surface was assumed with an emissivity of 0.95 with a 5% reflectivity. The energy applied was approximately 2 kJ over an inspection area of 200 mm × 200 mm. The pixel pitch is 0.32 mm.

A group of ten same samples mounted on a black foam plate were inspected (see Figure 6(c)). Figure 7(a) shows a raw temperature thermogram (the sixth frame after the flash) of the test board inspected from the top side. By extracting the temperature response of center points, Figure 7(b) presents the temporal profile of each sample within one-second post flash. It illustrates a small difference between each sample in temperature peak and decays after one pulse flash. The experimental results can not only verify the simulation model but also provide realistic data to help evaluate the experimental noises.

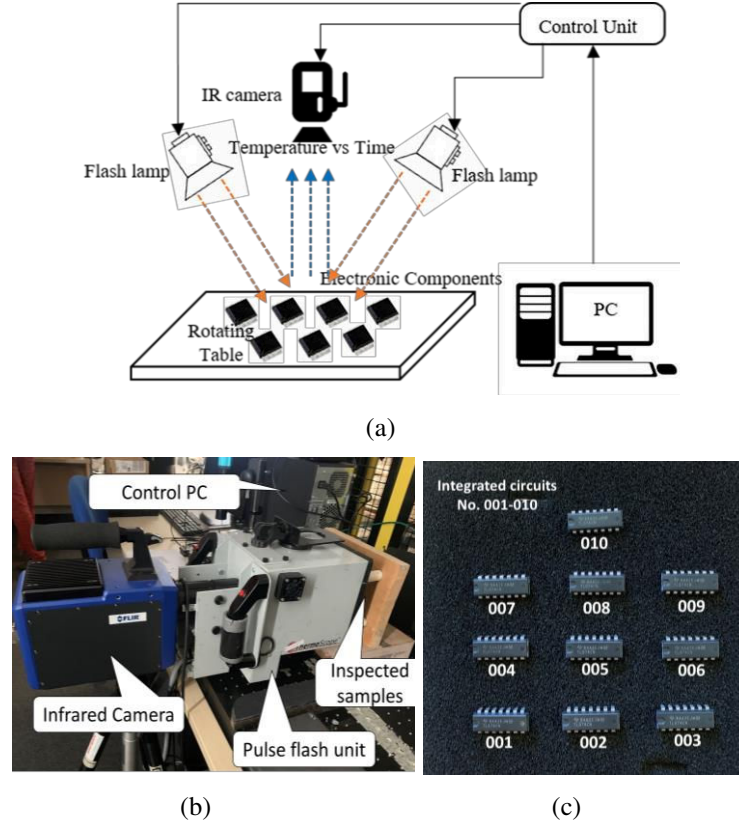


Figure 6. System framework. (a) Experimental configuration of the PT inspection; (b) A snapshot of the experimental system; (c) The layout of EC samples in the experiment

The temperature distribution of the model and the results of center slice at 0.02 second are shown in Figure 8(a), which presents a clear temperature distribution and penetration through the mould compound to the die layer. After obtaining the experimental results, a region of interest (ROI) is extracted for further analysis to compare the simulation and experimental data. Figure 8(b) presents the time evolution of transient temperature profiles at the center point location of the simulated model and the samples No.1, No.2 and No.5. Figure 8(c) shows the temperature spatial distribution of four different time stamps at the centerline shown in Figure 8(a). The experimental results demonstrate that the results agree with the predictions of both the temporal and spatial profile of the EC provided by the simulation model. Based on the simulation results and respective comparison, the reference values of our three target parameters are tabulated in Table 2, which will be regarded as the genuine

references to investigate the detectability of parameter deviation. To briefly describe the three attributes deviation mentioned above, conductivity, volumetric heat capacity and die size will be used in the sections below. And also “anomaly” will be used to denote the attributes deviation below, unless specified otherwise.

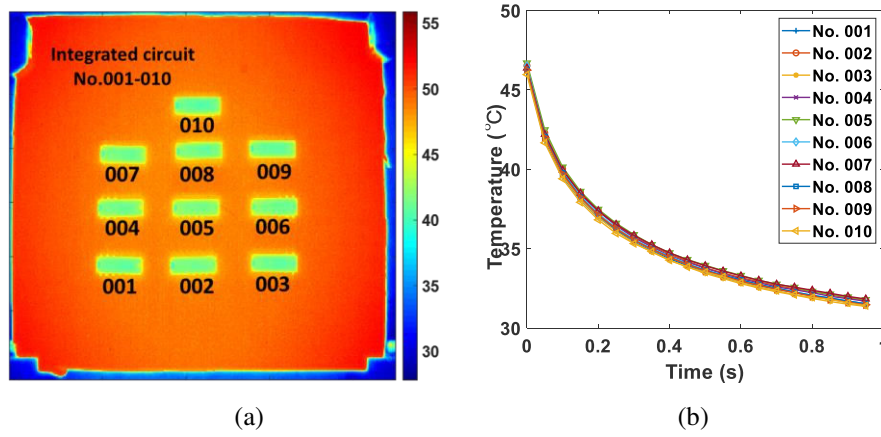


Figure 7. Experimental results. (a) A raw temperature image after flash (Frame 6); (b) Temperature profile of the center point of each sample.

To obtain the thermal response more practically, experimental temporal noise was analysed and then introduced to the simulated response. Shepard [17] proposed a Thermal Signal Reconstruction (TSR) technique to reduce temporal noise using a high order polynomial model to fit the temperature cooling curve. The model can be written as Eq. (4):

$$\ln[T(t)] = \sum_{i=0}^N a_i \ln[T(t)]^i \quad (4)$$

where $T(t)$ is the surface temperature at time t , N is the model order, and a_i are coefficients to be estimated. Once the unknown coefficient a_i is estimated by the least square method, the temperature behaviour can be reconstructed to replace the raw data. Then both raw data and reconstructed data were compared to calculate the SNR using Eq. (5), where T_{expt} and T_{poly} denote the experimental signal and TSR signal, respectively. After calculation of all samples, the results indicate that the mean SNR for these samples is around 64dB. To ensure the stability of experiments, all ten samples were retested one-by-one in the same environment

and the SNR of the surface temperature signal was evaluated by TSR respectively. The SNR values of the five samples are shown in Figure 8(d). Considering the uncertainty occurring due to multiple tests or operators, random noises with an SNR of 60dB (averaged noise in experiments is around 64dB) was introduced into the simulated temperature response to represent the results of multiple samples in one inspection.

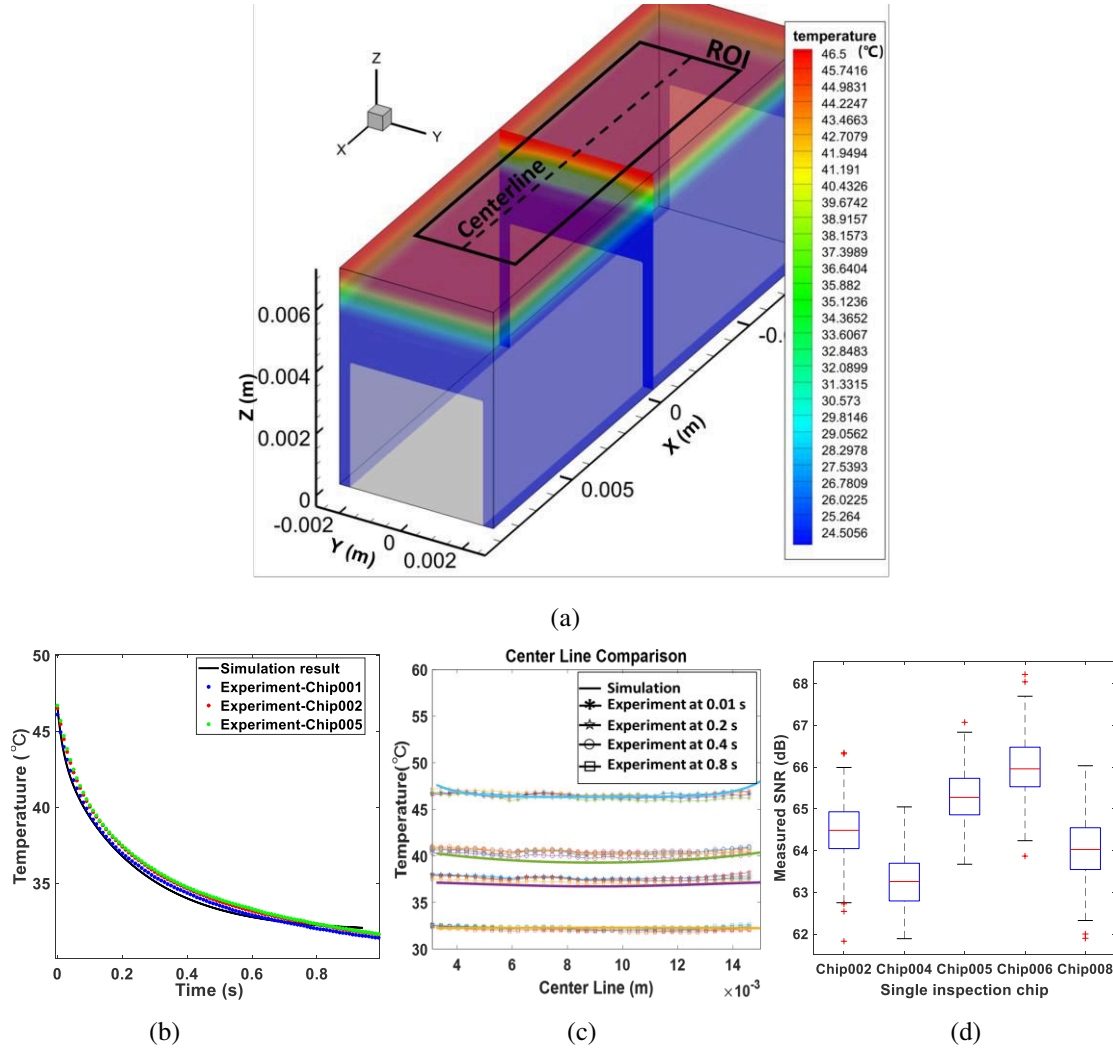


Figure 8. Comparison between simulated and experimental results. (a) The simulated results of model at 0.02s; (b) Comparison of center point transient temperature profiles; (c) Centerline temperature distribution of four different time stamps. (d) The error bar surface temperature of experiments.

$$SNR = 20 \cdot \log_{10} \frac{rms T_{expt}}{rms(T_{expt} - T_{poly})} \quad (5)$$

Table 2 reference value of three target parameters

Anomalous parameters	Conductivity	Volumetric heat capacity	Die size
Reference value	7.2 W/(m·K)	1.33×10^6 J/K/m ³	9.0 mm × 3.0 mm×0.6 mm

3. Detectability Estimation Using Machine Learning Classification

3.1 Feature extraction

To reveal the variation of thermal response that could be caused by counterfeit parts, Principal Component Analysis (PCA) is used for the extraction of the spatial and temporal information from a thermographic matrix formed by an image sequence. PCA has been shown to yield high levels of thermal contrast for underlying structural damage resulting in satisfactory detectability compared to conventional thermographic procedures [35].

The Singular Value Decomposition (SVD) is a powerful method to compute the principal component analysis. In general, the SVD of an $M \times N$ matrix A ($M > N$) is a factorisation of the following equation:

$$A = URV^T \quad (6)$$

where U is an $M \times N$ orthogonal matrix, R is a diagonal matrix (with the non-negative singular values of A on the diagonal) and V^T is the transpose of an $N \times N$ orthogonal matrix. The thermal image sequence is arranged in a form of the time steps as the column-wise and the pixels as the row-wise of A . And the columns of decomposed U comprise the orthogonal statistical modes known as Empirical Orthogonal Functions (EOF) which describes the spatial variation in the thermograms. Likewise, the Principal Components (PCs), which describes the temporal variation, comprises the rows in matrix V^T . Commonly, the first two orders of EOFs and PCs provide sufficient description of data variability in space and time domain.

In this research, the purpose is to identify the anomaly level in the bulk material and die size which affects the temperature response of the entire surface more evidently rather than a region on the surface. In PT, the flash covers the entire heating surface of ECs in which the main thermal transfer occurs along the depth direction. To evaluate the representation ability for a counterfeit-introduced anomaly using PCs as the features, three gross-graded groups of parametric error models are generated for representing three types of attributes. Regarding the reference value of three parameters as the genuine value, the gross-graded error models consisting of nine bias of each parameter starts from -40% to +40% with an equivalent interval of 10%.

After simulating all models, the SVD was performed on the modelled temperature image sequence without noise to obtain the PCs. For conductivity, Figure 9 (a) and (b) respectively shows the transient curve of 1st PCs and 2nd PCs of the anomaly models. The 1st and 2nd PCs

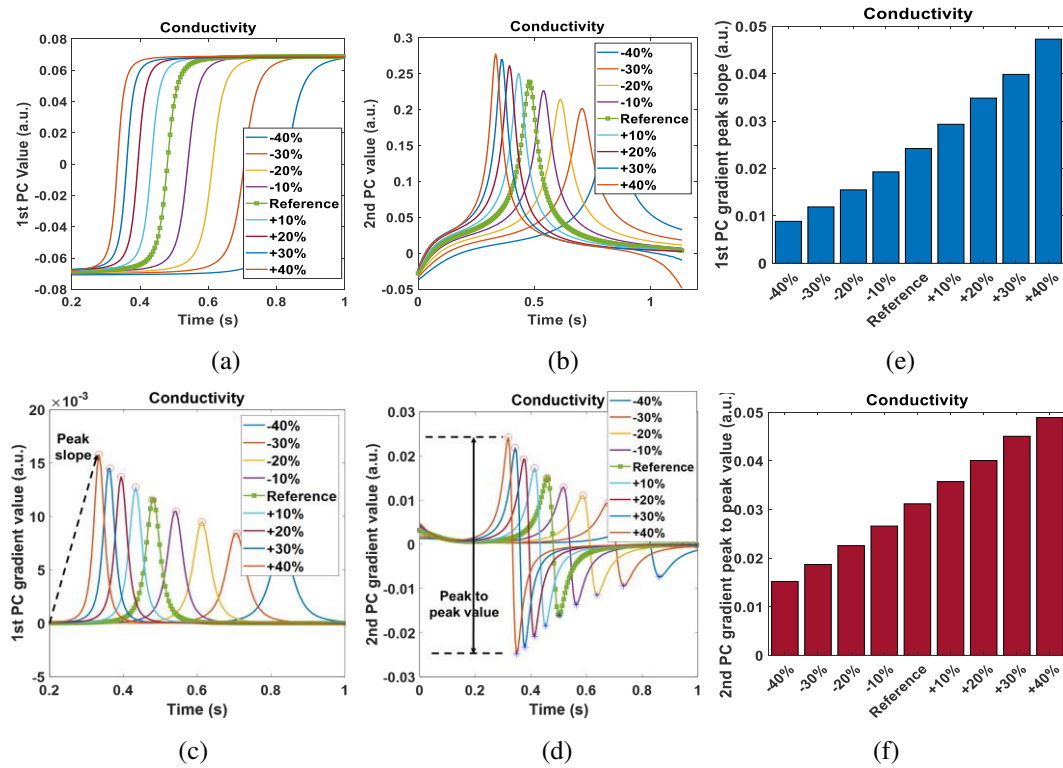


Figure 9. The results of PCA results and feature extraction of conductivity. (a) The 1st PCs profiles; (b) The 2nd PCs profiles; (c) The gradient of 1st PCs; (d) The gradient of 2nd PCs; (e) No.1 feature of the peak slope of 1st PCs; (f) No.2 feature of the peak to peak value of 2nd PCs;

can easily distinguish differences between the models. From the gradient graph of the 1st PCs shown in Figure 9(c), it can be observed that the 1st PC gradient curve has a single peak and the peak appears with higher amplitude and sharper with an increase in thermal conductivity. By defining the peak slope as the feature No.1, represented by the peak value dividing its respective time of appearance, Figure 9(e) shows that the No.1 feature exhibits increasing monotonicity with increasing conductivity. Figure 9(d) presents the gradients of the 2nd PCs. By selecting the peak-to-peak distance, which grows with an increase in conductivity, the No.2 feature (see Figure 9(f)) to describe the parameter variation is obtained.

Likewise, the 1st PCs and 2nd PCs of anomaly models for volumetric heat capacity were also analysed by PCA (see Figure 10(a) and 10(b)). The peak slope of the 1st PC gradients (see Figure 10(c)) and the peak-to-peak value of the 2nd PC gradients (see Figure 10(d)) were also selected as the double features for representing the anomaly. The bar charts of No.1 and

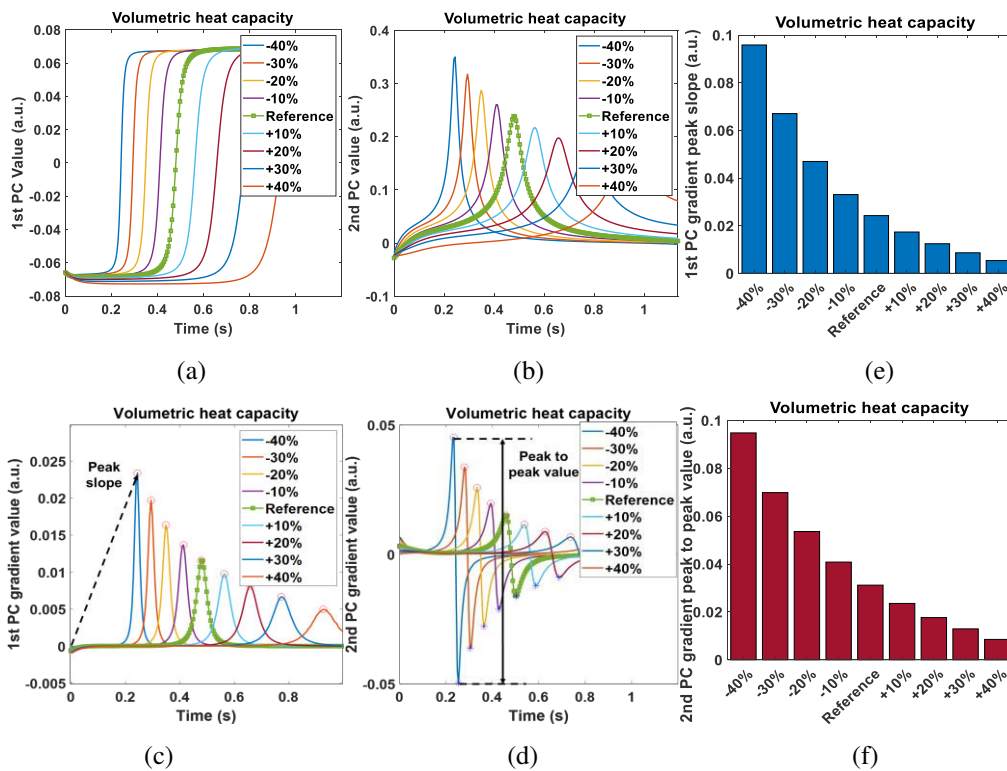


Figure 10. The results of PCA results and feature extraction of volumetric heat capacity. (a) The 1st PCs profiles; (b) The 2nd PCs profiles; (c) The gradient of 1st PCs; (d) The gradient of 2nd PCs; (e) No.1 feature of the peak slope of 1st PCs; (f) No.2 feature of peak to peak value of 2nd PCs;

No.2 features present clear decreasing monotonicity with the volumetric heat capacity growing which is consistent with the reciprocal relation between conductivity and the volumetric heat capacity. Viewing the feature trends of above two mould material anomalies, the No. 1 feature (peak slope) represents the time and the energy intensity when the excitation heat reaches the lead frame and die layers. The No.2 feature (peak-to-peak value) indicates the amount of heat penetrating through the mould and also the temperature rise of the die and lead layer. Similarly, the No.1 and No.2 features extracted from 1st and 2nd PC gradients (see Figure 11(c) and Figure 11 (d)) for die anomalous size models are presented in Figure 11(e) and Figure 11(f) respectively. Although the variation of features for die size anomalies are not as obvious as the other two parameters, they still maintain a linear relationship with parameter step change. For the anomaly of die size, similar physical reasoning can be applied. The No. 1 and No.2 features indicate that the temperature rise changes (e.g. significant

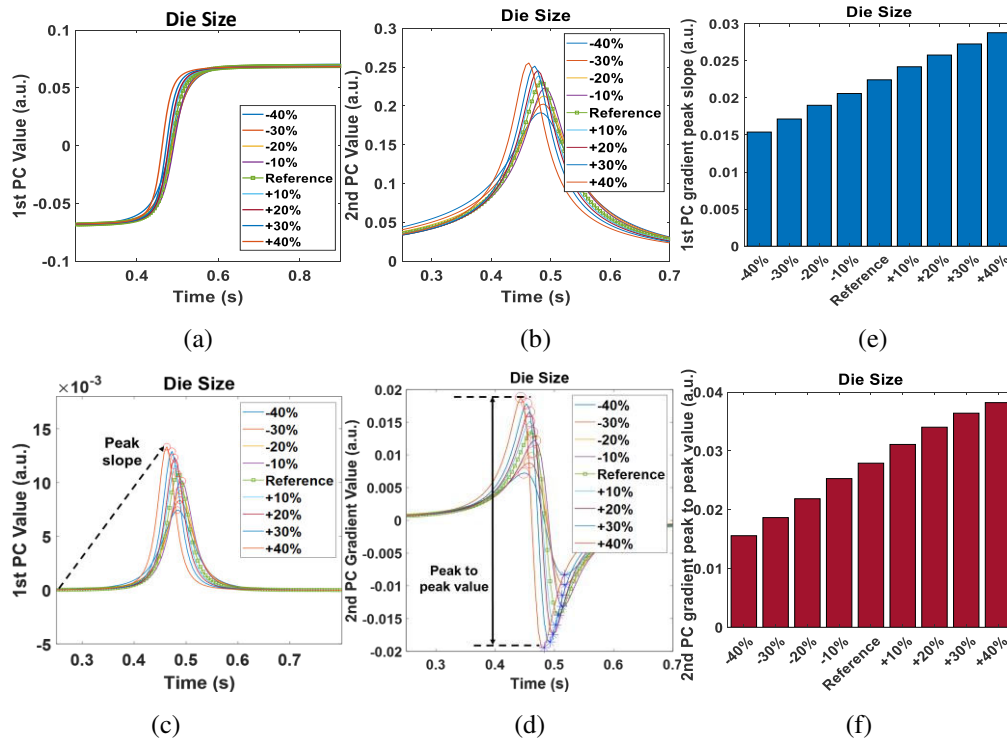


Figure 11. The results of PCA results and feature extraction of die size. (a) The 1st PCs profiles; (b) The 2nd PCs profiles; (c) The gradient of 1st PCs; (d) The gradient of 2nd PCs; (e) No.1 feature of the peak slope of 1st PCs; (f) No.2 feature of the peak to peak value of 2nd PCs;

amplitude changes of two features) at the die layer when the same amount of heat reaches the die at almost the same time (e.g. not significant time changes of two features).

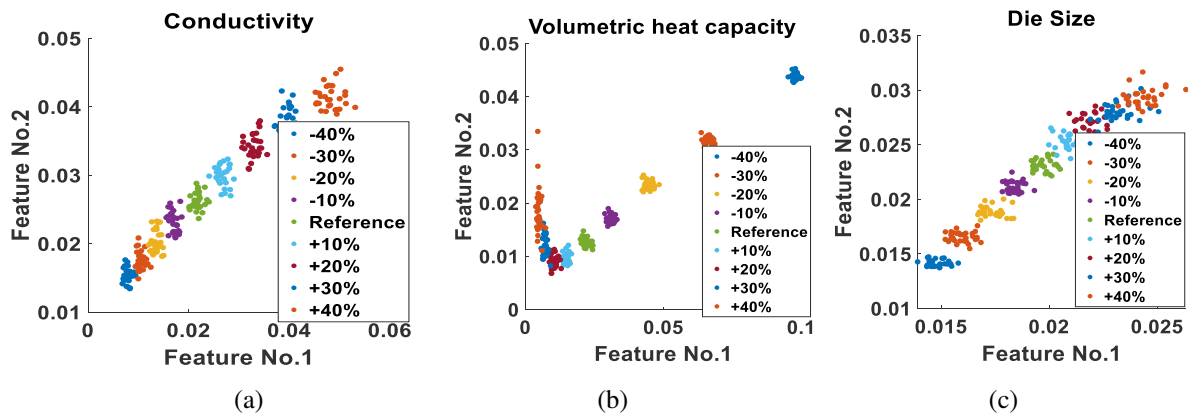


Figure 12. The scatter distribution of No.1 feature and No.2 feature of three parameters. (a) Conductivity; (b) Volumetric heat capacity; (c) Die size;

Based on the analysis above, all noised data of anomaly models were analysed to obtain the features. As shown in the scatter plot of double features in Figure 12 (a), (b) and (c), the scattered dots of double features for each noised anomalous model are grouped together in terms of the value of each parameter. This demonstrates a strong potential to perform detectability estimation by clustering the feature points using machine learning classification approaches. To more finely characterise anomaly detectability based on the genuine reference model, finer anomalous levels are necessary, and the target focus should be on the classification of different features of counterfeit and genuine models, respectively.

3.2 Detectability estimation using machine learning classification

After the identification of important features, this paper proposes to use support vector machine (SVM), a popular machine-learning-based supervised classification method, to determine if two feature groups generated by different values of a certain parameter (e.g. conductivity) can be distinguished. It should be noted that other methods, such as KNN or decision tree, can also be applied. SVM was selected due to its fine performance and wide

applicability. Cross-validation is employed in this paper to evaluate the classification performance. The data were initially divided into N folders, and $N - 1$ folders are then selected for the training and the remaining folder was utilised for the testing requirement. This step is repeated N times until each folder has been used for the testing, and the accuracy is finally averaged. Cross-validation combines measures of fitness in prediction to derive a more accurate estimate of model prediction performance [36]. In this paper, 10-fold cross-validation was used. If the classification accuracy between the reference group and the testing group is larger than a certain threshold, the parameter value of the testing group is determined as “detectable”, otherwise marked as “undetectable”. By this means, the detectability from the variation of each parameter can be detected. For this work, the threshold was set at 90%. The proposed strategy of detectability estimation can be summarised as:

- (1) Establish the feature database of the anomaly models where various deviations of each parameter from the reference are tested;
- (2) Separate the database into training and validation sets using 10-fold cross-validation;
- (3) Train a series of binary classifiers between each anomaly model and the reference model using the SVM algorithm;
- (4) Calculate the classification accuracy of each classifier on the validation set;
- (5) Repeat step 2) to 5) until every folder of data has been selected as the validation set and the classification accuracy is averaged;
- (6) Define a threshold of classification accuracy to determine the detectability. If the accuracy for an anomalous level is larger than the threshold, this anomaly level of the parameter is regarded as detectable. Otherwise, this level will be decided as undetectable;
- (7) Identify the largest level of parameter deviation as the estimated detectability range.

4. Results and discussion

As mentioned in Section 3.2, the detectability of the mould material and the die's structural attributive anomaly can be estimated by the clustering approach. To accurately obtain the detectability level, a finer graded anomaly group using an equal interval level in the log domain from -10% to +10% deviation was applied on the reference values of three parameters to make three corresponding counterfeiting sets. Each set consists of 30 anomaly models and a reference model. All models were then simulated using the proposed FEM. Thermal response data of each anomaly model was added with noise with an SNR of 60dB for 40 times to generate the raw dataset for detectability estimation. In total, 1240 feature pairs (31 anomaly models multiplied by 40 noised cases) were available for each counterfeit parameter. As shown in Figure 13 (a), (c) and (e), the feature space of three anomaly datasets from -5% error model to +5% error model are described in the box chart. The statistics analysis was conducted on the 40 times repeated addition of noise. It can be seen that the trends of two features in the box chart are consistent on the monotonicity obtained in the feature extraction section. Also, the box chart exhibits clear data overlapping of feature points between anomaly models. This phenomenon indicates that the smaller the anomalous level is, the feature datasets will locate closer to the data of the reference model. This means it will be more difficult to differentiate them from the reference model.

In addition, to ensure the SVM is the best clustering algorithm in this scenario, the comparison of classification accuracy from K-Nearest Neighbor (KNN), Linear Discriminant Analysis (LDA), Decision Tree (DT) and SVM algorithms are presented in Table 3. Several anomaly levels are selected to observe the accuracy differentiation and the best results for each level are highlighted in bold in Table 3. It can be observed that the SVM can acquire the

best cluster accuracy in most cases demonstrating the superiority of SVM over other common clustering algorithms.

Table 3 classification accuracy of different algorithm.

Anomaly level	KNN	LDA	DT	SVM
+1%	60.00%	63.75%	53.75%	65.00%
-1%	61.25%	68.25%	55.00%	71.25%
+2.57%	88.75%	92.50%	80.00%	90.00%
-2.57%	88.75%	85.00%	86.25%	88.75%
+3.01%	93.75%	95.00%	87.50%	96.25%
-3.01%	83.75%	87.50%	82.50%	87.50%

Within 40 groups of data for each model, the results of classification accuracy for three parameters were then acquired, as presented in Figure 13(b), Figure 13(d) and Figure 13(f) respectively. These results demonstrate that the accuracy approaches 100% when the model anomalies exceed 5% of the references, thus demonstrating the capability, reliability and the success rate of detecting anomalies within these ranges using PT. With the anomaly error level decreasing, the accuracy decreases, indicating that the detectability follows closely. Setting a 90% of classification accuracy as the detectable threshold, the detectable range for the three parameters can be observed from Figure 13(b), Figure 13(d) and Figure 13(f). In addition, it can be observed that, unlike the parameters' errors distribution, the accuracy distribution of anomaly models is not symmetric. This is due to how the positive and negative errors of each parameter influence the heat transfer behaviour of the whole component, yielding differences which are inherently asymmetric. For example, the positive error of mould thermal conductivity means improved heat transfer capability. The same level of noise will lead to a smaller influence on the result than the lower heat transfer models represented by the negative error. Therefore, the detectability for conductivity on the positive error is greater than the negative error. Similar explanations are also applicable to the parameters of volumetric heat capacity and the die size. The detectable range of three anomaly parameters

is summarised in Table 4. These results have demonstrated the feasibility of the proposed method to characterise the detectability of several materials and interior structural counterfeits in ECs, providing a reasonable and clear pathway for detectability estimation based on the combination of simulation modelling and machine learning classification, instead of collecting thousands of standardised CEC samples.

It should be noted that the detectable range for the counterfeit is based on the ECs and the 90 % threshold set. In practice, the range will vary from different ECs and the threshold used. A more restricted tolerance will result in a lower detectability. The strategy of optimal threshold selection should be analysed in future research based on sufficient prior knowledge from manufacturing and quality control process, from which the detectability result will be more meaningful in return.

Following these results, some issues and alternatives require consideration. One aspect of the problem provides that the material and inner structural anomalies of CECs may

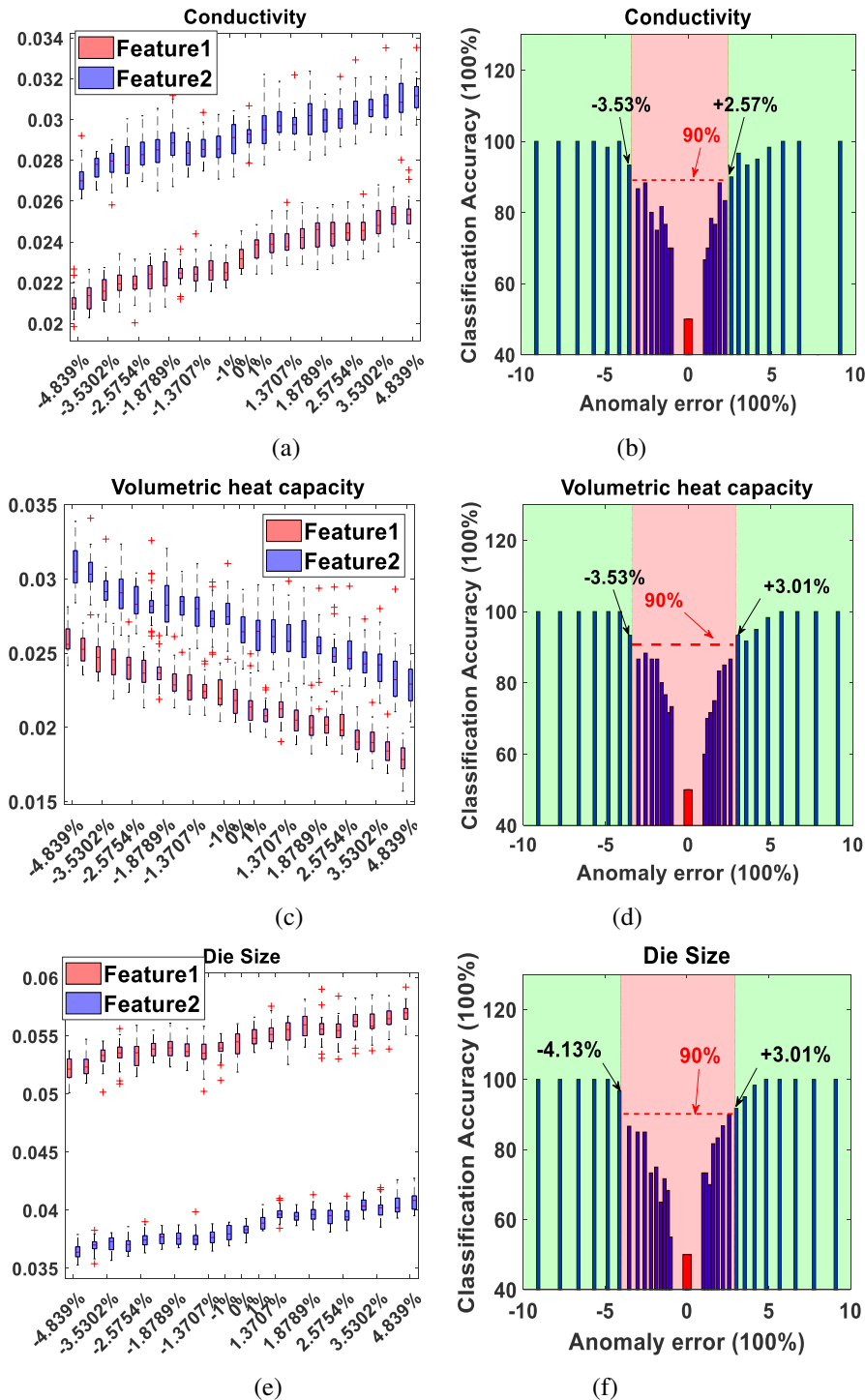


Figure 13. The feature spaces and estimated detectability range of three counterfeit parameters. (a) The feature trends of conductivity in box chart; (b) The estimated detectability of conductivity; (c) The feature trends of volumetric heat capacity in box chart; (d) The estimated detectability of volumetric heat capacity; (e) The feature trends of die size in box chart; (f) The estimated detectability of die size.

significantly vary from different types of counterfeit. In this circumstance, as a supervised machine learning methodology, the features extracted from PCA may not exactly match with those used in this paper (peak slope of 1st PCs and peak-to-peak value of 2nd PCs). For detection of counterfeits with local defects (i.e. fake surface coating or missing wire counterfeits), the features from EOFs which mainly represent spatial variance will be more effective for machine learning classification.

In order to extend its suitability for multiple types of EC, the selection and optimisation of PT inspection parameters and modelling various inspection problems contribute to the assessment of the desired detection capability. For larger and thicker components, higher pulse energy and longer heating duration should be selected to ensure sufficient induced power and resulting thermal behaviour being captured. Meanwhile, the data capture method referring to sampling rate, ROI and the temperature decay sections corresponding to different ECs and pulse modes should be investigated further, as inspection parameters have a significant impact on the quality of data for performing the target inspection.

The proposed method explores the detection feasibility using PT for CECs. Due to the features of PT, it provides a powerful and cost-efficient technique for the first stage large scale screening to reduce the proliferation of counterfeits. Based on the numerical simulation, the surface thermal signals of multiple standardised levels of anomalous ECs can be predicted before gathering and inspecting the large quantity of counterfeit chips. It furtherly simplifies the evaluation procedure and promotes detectability resolution. In addition, the machine learning decision-making strategy can provide operators with a fast and stable decision which is also very suitable for the inspection scenario of large quantity screening. However, it should be noted that the visualisation resolution and detectability of PT for small internal defects (e.g. missing or broken wires, electrical malfunction die) are not as high as other

techniques like X-Ray or THz testing with strong penetration capability. A combination of the proposed method with these methods could better balance the inspection time and accuracy.

Table 4 The detectability range

Counterfeit parameter	Reference value	Detectable range of anomaly
Mould heat conductivity	7.2 W/(m·K)	Error > -3.53% or +2.57%
Mould volumetric heat capacity	1.33×10 ⁶ J/K/m ³	Error > -3.53% or +3.01%
Die size	9.0 mm × 3.0mm × 0.6 mm	Error > -4.13% or +3.01%

5. Conclusions

Different from most of PT related researches targeting on damage/defect characterisation, this paper is aimed at investigating its feasibility of the detection of CECs. In this research, a detectability estimation approach was proposed to identify the detectable limits of the material and its inner structural anomalies in CECs based on thermal transfer FEM simulation approach. The results show the following.

- (1) FEM simulation can effectively predict the transient thermal response signal of electronic components in the PT inspection. Furthermore, the simulation approach can provide the multiple inspection signals which come from standardised levels of an anomaly in material and structural counterfeit components. Compared to experimental testing, a significant amount of standardised counterfeit samples are not required.
- (2) For the anomalies in the mould compound material and die structure, by using PCA, the first two PCs are strongly correlated with three parameters of mould compound thermal conductivity, volumetric heat capacity and inner die size. It has been observed that the peak slope of the 1st PCs gradient curve and the peak-to-peak value of the 2nd PCs gradient curve have good monotonicity with changing of the above three parameters. This observation allows deriving a categorisation scenario of the anomaly features to

represent the variation of each anomaly model, which enables the quantitative estimation of detectability using a supervised machine learning classification approach.

- (3) Machine learning classification based on the support vector machine algorithm can successfully detect the detectable range of investigating counterfeit anomaly when an appropriate classification accuracy threshold is selected.
- (4) The proposed framework can effectively assess the detectability of material and structural anomalies based on the decision making of machine learning classification. The detectable range for mould compound conductivity anomaly is greater than -3.53% or +2.57% error, and for the mould compound, the volumetric heat capacity is greater than -3.53% or +3.01% error. The detectable range for die size is larger than -4.13% with a +3.01% error.

It should be noted that this is a feasibility study. To fully explore its potential and improve the versatility, a further study is required by accurately modelling the detailed inner material and structures for different types of ECs. In addition, as a data-driven approach based on machine learning, it is also necessary to emphasise that simulation is a more straight-forward method for data accumulation than the real case. Also, as some difficulty in collecting a sufficient number of CECs with standardized defects from customers, manufacturers and even from gray market can be expected. The experiment investigation should be implemented with a sufficient volume of CEC examples with support from manufacturers and active participants in the electronic parts supply chain.

Acknowledgement

This work was partly supported by the Lloyd's Register Foundation under Grant number GA\100113, and partly supported by the UK EPSRC Platform Grant: Through-life performance: From science to instrumentation (Grant number EP/P027121/1).

References

- [1] OECD/EUIPO, Trends in Trade in Counterfeit and Pirated Goods, Illicit Trade, OECD Publishing, Paris, 2019.
- [2] "Annual IP crime and enforcement report: 2017 to 2018", GOV.UK, 2019. [Online]. Available: <https://www.gov.uk/government/publications/annual-ip-crime-and-enforcement-report-2017-to-2018>. [Accessed: 30- Sep- 2019].
- [3] H. Livingston, Avoiding counterfeit electronic components, IEEE T. COMP. PACK. MAN., 30 (2017) 187-189.
- [4] U. Guin, K. Huang, D. DiMase, J. M. Carulli, M. Tehranipoor, and Y. Makris, Counterfeit Integrated Circuits: A Rising Threat in the Global Semiconductor Supply Chain, Proc. IEEE, 102 (2014) 1207-1228.
- [5] M. Pecht and S. Tiku, Bogus: electronic manufacturing and consumers confront a rising tide of counterfeit electronics, IEEE Spectrum., 43 (2006) 37-46, 2006.
- [6] U. Guin, D. DiMase and M. Tehranipoor, Counterfeit Integrated Circuits: Detection, Avoidance, and the Challenges Ahead, J. Electron. Test., 30 (2014) 9-23.
- [7] Xuehui Zhang and M. Tehranipoor, Design of On-Chip Lightweight Sensors for Effective Detection of Recycled ICs, IEEE Trans. Vlsi. Syst., 22 (2014) 1016-1029.
- [8] B. Jamshidieini and R. Fazaee, Detecting defective electrical components in heterogeneous infra-red images by spatial control charts, Infrared. Phys. Techn., 76 (2016) 510-520.
- [9] U. Guin and M. Tehranipoor, On Selection of Counterfeit IC Detection Methods. 2013.
- [10] C. Benedek, O. Krammer, M. Janoczki, L. Jakab, Solder Paste Scooping Detection by Multilevel Visual Inspection of Printed Circuit Boards, IEEE Trans. Ind. Electron., 60 (2013) 2318-2331.

- [11] M. Alam, H. Shen, N. Asadizanjani, M. Tehranipoor, D. Forte, Impact of X-Ray Tomography on the Reliability of Integrated Circuits, *IEEE Trans. Device mat. Re.*, 17 (2017) 59-68.
- [12] K. Ahi, S. Shahbazmohamadi, N. Asadizanjani, Quality control and authentication of packaged integrated circuits using enhanced-spatial-resolution terahertz time-domain spectroscopy and imaging, *Optics and Lasers in Engineering*. 104 (2018) 274-284.
- [13] Laung-Terng Wang. Charles E. Stroud. Nur A. Touba., Laung-Terng Wang., *System-on-chip Test Architectures: Nanometer Design for Testability*, Morgan Kaufmann Publishers, 2008.
- [14] U. Guin, X. Zhang, D. Forte and M. Tehranipoor, Low-cost on-chip structures for combating die and IC recycling, 2014 51st ACM/EDAC/IEEE Design Automation Conference (DAC), San Francisco, CA, (2014) 1-6.
- [15] R. Patti, Three-Dimensional Integrated Circuits and the Future of System-on-Chip Designs, *P. IEEE*, 94 (2006) 1214-1224.
- [16] J. Tachapitunsuk, K. Ugsornrat, W. Srisuwitthanon, and P. Thonglor, Effecting aging time of epoxy molding compound to molding process for integrated circuit packaging, *Siam Physics Congress 2017*, 901 (2017).
- [17] M. S. Jadin and S. Taib, Recent progress in diagnosing the reliability of electrical equipment by using infrared thermography, *Infrared. Phys. Techn.*, 55 (2012) 236-245.
- [18] S. M. Shepard, *Advances in pulsed thermography (Aerospace/Defense Sensing, Simulation, and Controls)*. SPIE, (2001).
- [19] H. C. Liu, C. X. Pei, J. X. Qiu, and Z. M. Chen, Inspection of Delamination Defect in First Wall Panel of Tokamak Device by Using Laser Infrared Thermography Technique, *IEEE Trans. Plasma. Sci.*, vol. 46, no. 7, pp. 2699-2707, 2018.

- [20] Li, K., Tian, G., Cheng, L., Yin, A., Cao, W. and Crichton, S., State Detection of Bond Wires in IGBT Modules Using Eddy Current Pulsed Thermography. *IEEE Trans. Power Electr.*, 29 (2014) 5000-5009.
- [21] X. Liu, G. Tian, Y. Chen, H. Luo, J. Zhang, W. Li, Non-Contact Degradation Evaluation for IGBT Modules Using Eddy Current Pulsed Thermography Approach, *Energies*. 13 (2020) 2613.
- [22] A. Sirikham, Y. Zhao, H. Nezhad, W. Du and R. Roy, Estimation of Damage Thickness in Fiber-Reinforced Composites using Pulsed Thermography, *IEEE Trans. Ind. Informat.*, 15 (2019) 445-453.
- [23] Y. Zhao, J. Mehnen, A. Sirikham and R. Roy, A novel defect depth measurement method based on Nonlinear System Identification for pulsed thermographic inspection, *Mech. Syst. Signal Pr.*, 85 (2017) 382-395, 2017.
- [24] H. Liu, C. Pei, S. Xie, Y. Li, Y. Zhao, Z. Chen, Inversion Technique for Quantitative Infrared Thermography Evaluation of Delamination Defects in Multilayered Structures, *IEEE Trans. Ind. Informat.*, 16 (2020) 4592-4602.
- [25] Wang, Z., Zhu, J., Tian, G. and Ciampa, F., Comparative analysis of eddy current pulsed thermography and long pulse thermography for damage detection in metals and composites. *NDT&E Int.*, 107 (2019) 102-155.
- [26] L. Choobineh and A. Jain, Analytical Solution for Steady-State and Transient Temperature Fields in Vertically Stacked 3-D Integrated Circuits, *IEEE Trans. Comp. Pack. Man.*, 2 (2012) 2031-2039.
- [27] L. Choobineh and A. Jain, An explicit analytical model for rapid computation of temperature field in a three-dimensional integrated circuit (3D IC), *Int. J Therm. Sci.*, 87 (2015) 103-109.

- [28] G. Susto, A. Schirru, S. Pampuri, S. McLoone and A. Beghi, Machine Learning for Predictive Maintenance: A Multiple Classifier Approach, *IEEE Trans. Ind. Informat.*, 11 (2015) 812-820, 2015.
- [29] A. Noori Hoshyar, M. Rashidi, R. Liyanapathirana and B. Samali, Algorithm Development for the Non-Destructive Testing of Structural Damage, *Appl. Sci-Basel*, 9 (2019) 2810.
- [30] Z. Tong, S. Xie, X. Li, C. Pei, Z. Chen and Y. He, Efficient numerical simulation of eddy current pulsed thermography NDT signals based on FEM-BEM method and energy equivalent principle, *Infrared. Phys. Techn.*, 101 (2019) 138-145.
- [31] S. Wirtz, N. Beganovic and D. Söffker, Investigation of damage detectability in composites using frequency-based classification of acoustic emission measurements, *Struct. Health Monit.*, 18 (2018)1207-1218, 2018.
- [32] K. Ahi, A method and system for enhancing the resolution of terahertz imaging, *Measurement*. 138 (2019) 614-619.
- [33] T. Aujeszky, G. Korres, and M. Eid, Material classification with laser thermography and machine learning, *Quant. Infr. Therm. J.*, 16 (2019) 181-202.
- [34] H. Liu, S. Xie, C. Pei, J. Qiu, Y. Li, Z. Chen, Development of a Fast Numerical Simulator for Infrared Thermography Testing Signals of Delamination Defect in a Multilayered Plate, *IEEE Trans. Ind. Informat.* 14 (2018) 5544-5552.
- [35] V. Feuillet, L. Ibos, M. Fois, J. Dumoulin and Y. Candau, "Defect detection and characterization in composite materials using square pulse thermography coupled with singular value decomposition analysis and thermal quadrupole modeling", *NDT&E Int.*, vol. 51, pp. 58-67, 2012.

- [36] G. Seni and J. Elder, "Ensemble Methods in Data Mining: Improving Accuracy Through Combining Predictions", *Synthesis Lectures on Data Mining and Knowledge Discovery*, vol. 2, no. 1, pp. 1-126, 2010.

Detectability evaluation of attributes anomaly for electronic components using pulsed thermography

Liu, Haochen

2020-09-16

Attribution-NonCommercial-NoDerivatives 4.0 International

Liu H, Tinsley L, Addepalli S, et al., (2020) Detectability evaluation of attributes anomaly for electronic components using pulsed thermography. *Infrared Physics and Technology*, Volume 111, December 2020, Article number 103513

<https://doi.org/10.1016/j.infrared.2020.103513>

Downloaded from CERES Research Repository, Cranfield University